CryoEM reconstructions of membrane proteins solved in several amphipathic solvents, nanodisc, amphipol and detergents, yield amphipathic belts of similar sizes corresponding to a common ordered solvent layer

Veronica Zampieri, Alexia Gobet, Xavier Robert, Pierre Falson, Vincent Chaptal

▶ **To cite this version:**

Veronica Zampieri, Alexia Gobet, Xavier Robert, Pierre Falson, Vincent Chaptal. CryoEM reconstructions of membrane proteins solved in several amphipathic solvents, nanodisc, amphipol and detergents, yield amphipathic belts of similar sizes corresponding to a common ordered solvent layer. Biochimica et Biophysica Acta:Biomembranes, 2021, 1863 (11), pp.183693. 10.1016/j.bbamem.2021.183693 . hal-03453888

HAL Id: hal-03453888
https://hal.science/hal-03453888

Submitted on 16 Dec 2021

HAL is a multi-disciplinary open access archive for the deposit and dissemination of scientific research documents, whether they are published or not. The documents may come from teaching and research institutions in France or abroad, or from public or private research centers.

L'archive ouverte pluridisciplinaire **HAL**, est destinée au dépôt et à la diffusion de documents scientifiques de niveau recherche, publiés ou non, émanant des établissements d'enseignement et de recherche français ou étrangers, des laboratoires publics ou privés.

Title: CryoEM reconstructions of membrane proteins solved in several amphipathic solvents, Nanodisc, amphipol and detergents, yield amphipathic belts of similar sizes corresponding to a common ordered solvent layer

Veronica Zampieri[1], Alexia Gobet[1], Xavier Robert[1], Pierre Falson[1], Vincent Chaptal[1*]

[1] Molecular Microbiology and Structural Biochemistry Laboratory (CNRS UMR 5086), University of Lyon, IBCP, 7, passage du Vercors, 69367 Lyon, France.

* To whom correspondence should be addressed. vincent.chaptal@ibcp.fr

Summary

To maintain membrane proteins soluble in aqueous solution, amphipathic compounds are used to shield the hydrophobic patch of their membrane insertion, which forms a belt around the protein. This amphipathic belt is seldom looked at due to the difficulty to visualize it. Cryo-EM is now offering this possibility, where belts are visible in 3D reconstructions. We investigated membrane proteins solved in nanodiscs, amphipols or detergents to analyze whether the nature of the amphipathic compound influences the belt size in 3D reconstructions. We identified belt boundaries in map-density distributions and measured distances for every reconstruction. We showed that all the belts create on average similar reconstructions, whether they originate from the same protein, or from protein from different shapes and structures. There is no difference among detergents or types of nanodisc used. These observations illustrate that the belt observed in 3D reconstructions corresponds to the minimum ordered layer around membrane proteins.

Keywords: Cryo-EM; membrane proteins; detergent belt; nanodisc; amphipols

1. Introduction

Membrane protein structure determination has taken a giant leap forward with the recent development of single particle electron microscopy in cryogenic conditions (Cryo-EM). Much more membrane protein structures become available [1, 2] (SFig. 1) improving our knowledge of many biological processes. In order to achieve this grail of a nice quality structure, it is necessary to extract the protein from the native membrane, and purify it to homogeneity so it can be applied on a grid and imaged on a microscope. And there lies the specificity of membrane proteins: they display a part of their structure that spans the membrane, abundant in hydrophobic residues, rendering them insoluble in water. There is thus a need for some amphipathic compound to shield this trans-membrane region from water and from other hydrophobic molecule or even other proteins around, else the result will be aggregation and loss of the precious sample.

Many recipes are available today to maintain membrane proteins in solution. The historical way, still very much used today, is to use detergents to extract membrane proteins from the membrane and then purify them in detergent solutions. Detergents are small molecules that display a hydrophilic head and a hydrophobic tail. Both moieties vary in nature, length and size allowing a large panel of possible screening for good conditions, and they are also sometimes used in mixtures[3]. By nature, detergents are very mobile and form a dynamic belt wrapping around the trans-membrane part of the protein[4]. Due to this dynamic property, detergents can have sometimes negative impacts on membrane proteins structure and function. Therefore, detergents with increased stabilizing properties have been more recently conceived for limiting such mobility either by having a design close to lipids (LMNG)[3, 5-7] or by generating specific interactions[8]. Also, their amphipathic nature is unique to stabilize given conformations. For example, the well-studied Lactose permease from *E. coli* (LacY) has been proven to be stabilized in the outward-facing conformation when purified in LMNG, while being in an occluded or inward-facing conformation in DMNG or DDM[9].

Other tools have been developed to forgo the need for detergents. Among them the derivation of the lipid A apolipoprotein engineered as a series of Membrane Scaffold Proteins (MSP), that together with lipids and the membrane protein will form a lipidic nanodisc is a real success. It allows to reconstitute a more native environment and/or to vary the type of lipids around the membrane protein[10]. In the same vein, amphipols are polymers that wrap around purified membrane proteins and stabilize them without the need for detergents and lipids[11, 12]. All these tools have been used for membrane protein structure determination by Cryo-EM. More recently, new polymers have been designed to directly extract membrane proteins from native membranes, allowing their purification without detergents [13]. Also, several types of “lipid nanodiscs” originating from proteins, peptides or polymers have been described [14-17]. All these tools present advantages and limitations in their use, with extensive literature on each specific case (for example [18, 19]).

All these compounds generate a local amphipathic environment around the membrane region of membrane proteins that maintains them in aqueous solutions. This layer is a belt from which membrane proteins are indissociable. Importantly, all these environments bear intrinsic variability in size and shape as measured by various methods, alone or in complex with membrane proteins [18, 20-22]. Also, some environments like detergents are thought to be more fluid and displaying intrinsic variability [4] than more rigid ones like amphipols, know to stabilize membrane proteins for example [13]. Nonetheless, this solvent belt is seldom looked at despite its

huge influence on the protein function, due to the difficulty to visualize it. Cryo-EM now allows for the visualization of a layer wrapping around the transmembrane region of membrane proteins. We have taken this opportunity to investigate if there is an influence of these different amphipathic belts on their visualization after 3D reconstructions. We identified the position of the hydrophobic solvent belt in map-density distributions and measured the belts for many different proteins solved in nanodiscs, amphipols and detergents. We showed that all the belts create on average similar reconstructions, whether they originate from the same protein, or from protein from different shapes and structures. There is no difference amongst detergents or type of nanodisc used. These observations illustrate that the averaging procedure of CryoEM reconstructions returns a belt corresponding to a common minimum ordered solvent layer amongst all the membrane proteins particles selected for this reconstruction. This solvation layer is however smaller than the total amount of amphipathic compound embarked around membrane proteins.

2. Results

2.1. Selection and investigation of 3D reconstructions of membrane proteins structures solved by cryo-EM in several amphipathic belts

In order to discriminate whether there is an influence of the type of amphipathic belt on the 3D reconstructions used to image membrane proteins by cryo-EM, we have screened the whole Protein Data Bank to select for comparison the membrane proteins that have been solved only in multiple hydrophobic environments: nanodiscs, amphipols or detergents (Fig. 1A. and STable 1.). The idea behind this selection is to keep the protein fold constant in order to normalize its influence on the reconstruction, and to be able to focus on the solvent belts alone. For small membrane proteins like the ones selected in this study, trans-membrane helices dominate the reconstructions [23]. These reconstructions for proteins of similar folds will thus not be affected by protein's local structural changes, and warrants evaluating the effect of amphipathic belts on reconstructions. The identification of the belt is obvious to a trained eye, capable of detecting the trans-membrane parts of a protein in a structure. The hydrophobic belt is characterized by an expansion of lower-level density in the vicinity of the membrane region as a decrease in the map density. After the observation of map-density distributions of each structure of this dataset, an apparent feature was observable to identify the belt and is exemplified in Figure 1B. At high density levels, the very ordered parts of the structure are visible, on which reconstruction was anchored. Typically, trans-membrane helices are key features used in 3D reconstructions of membrane proteins and are visible at this level. With decreasing density levels, the number of voxels increases with the map-density distribution curve showing a concave shape (level 0). The higher ordered layers of the belt start to appear when the curve becomes convex (level 1, dotted arrow). The belt becomes more and more apparent over the course of about one log when the curve inflexes concavely (level 2) before a sharp increase in number of voxels leading to appearance of low-level noise throughout the box (level 3). Across all reconstructions, it is apparent that the more visible the hydrophobic belt, the clearer and sharper the transition is between levels 1 and 2. Notably, the hydrophobic belt inflates further away from the trans-membrane region as the map density decreases (transition from level 1 to level 2 in SFig. 2), which denotes different accuracy of belt visualization during reconstructions. The further away from the protein, the less homogeneous the belt is during the 3D reconstruction across a

particle dataset. We chose to measure distances at level 2 as it shows the full range of the belt (SFig. 3).

Importantly, most, if not all, published cryo-EM maps have been subjected to masking, and/or sharpening, and reconstructions could have been created with symmetry enforced, leading to slight distortions of the belt (STable 1). All these parameters, along with the type of software used, will have influence on the reconstruction and the size of the belt. Nevertheless, the final reconstruction is the one under scrutiny and subjected to analysis and comparison by outside investigators. With these restrictions in mind, the current analysis is still worth to get a grasp of amphipathic belt sizes across various reconstructions.

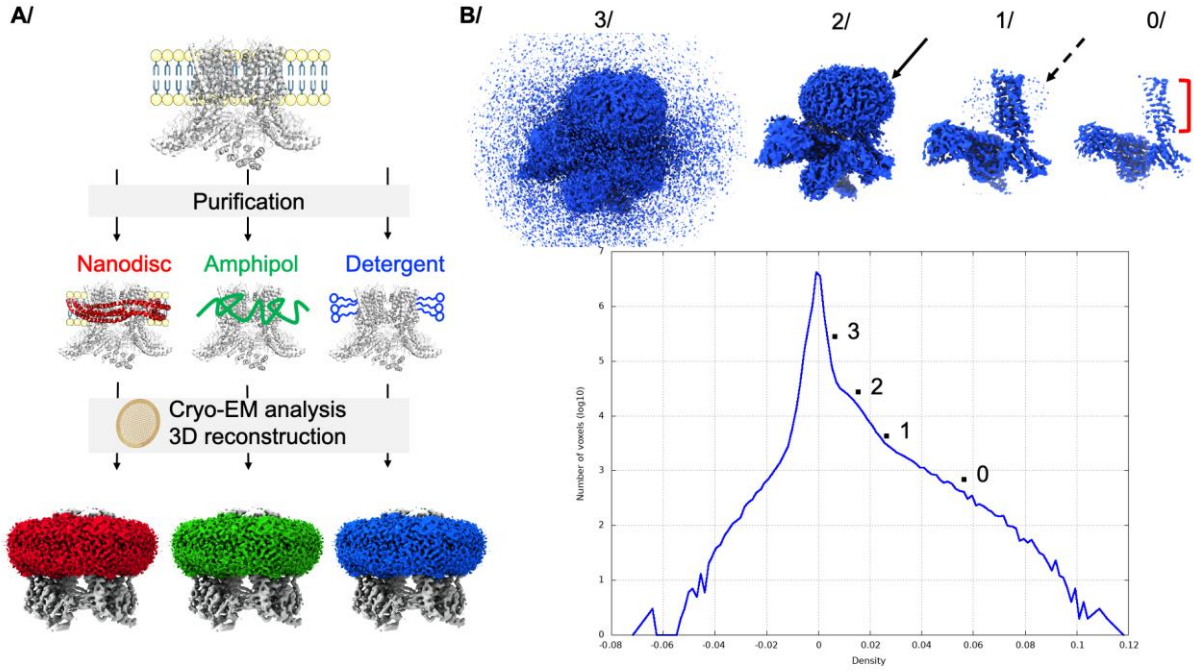

Fig. 1. Visualization of the different types of hydrophobic belts surrounding membrane proteins. **A/** General scheme of membrane protein purification from the membrane, kept in detergent (blue) or reconstituted in nanodisc (red) or amphipol (green), and imaged by cryo-EM to obtain a 3D reconstruction. The channel TRPV1 is used as an example of reconstruction (EMD-8117, PDB:5irx), with belts colored accordingly. **B/** Typical map-density distribution and representative density levels of reconstructions, using the muscarinic acetylcholine receptor/G-protein complex as an example (EMD-20079, PDB:6oik). Level 0 corresponds to parts of the structure with strong density; the red bar shows the trans-membrane domain. Level 1 corresponds to the appearance of high density for the belt, depicted by the dotted arrow. Level 2 represents the maximum density observed at low-level density, depicted by the solid arrow. Level 3 corresponds to low density noise.

2.2. 3D reconstructions of membrane proteins in nanodiscs or detergents yield similar average belt sizes

Using the map-density histogram, we measured for each entry the belt size by determining the distance between the protein edge and the solvent boundaries at level 2 (SFig. 4 to 18., STable 2.). Belt reconstructions are not completely spherical but rather follow the protein shape. We could thus identify long and short distances of the hydrophobic solvent belt, which we separated in two categories for further processing. Figure 2 displays the distance distribution plot of all proteins separated by hydrophobic environments: nanodiscs, amphipols and detergents. For each type of belt, there is an

apparent spread of distances, with 95% of total distances comprised between 14 and 36 Å, and no distances bellow 10 Å around the protein. Statistical analysis of long distances observed in detergents and nanodiscs show that they follow the same distribution, as well as small distances for these two categories. Considering the means for these two categories of amphipathic compound, the solvent belt is visible around the protein for 21 to 28 Å. The smaller number of structures solved using amphipols precludes the statistical analysis on means using parametric statistics. Non-parametric statistics on ranks reveals first an ambiguity about long amphipol distances where the current data set cannot distinguish whether the distances are different or similar to the nanodiscs or detergents ones (more measurements on more structures are needed to solve the debate). Second, it unambiguously state that short distances measured in amphipols follow the same distribution as the nanodiscs or detergents ones. Put together, these results point to a common average distance distribution of solvent belts surrounding membrane proteins observed after 3D reconstruction of cryo-EM data.

In order to distinguish if there is some inter-family of inter-solvent specificities hidden within the global distribution, we further separated proteins for individual analysis.

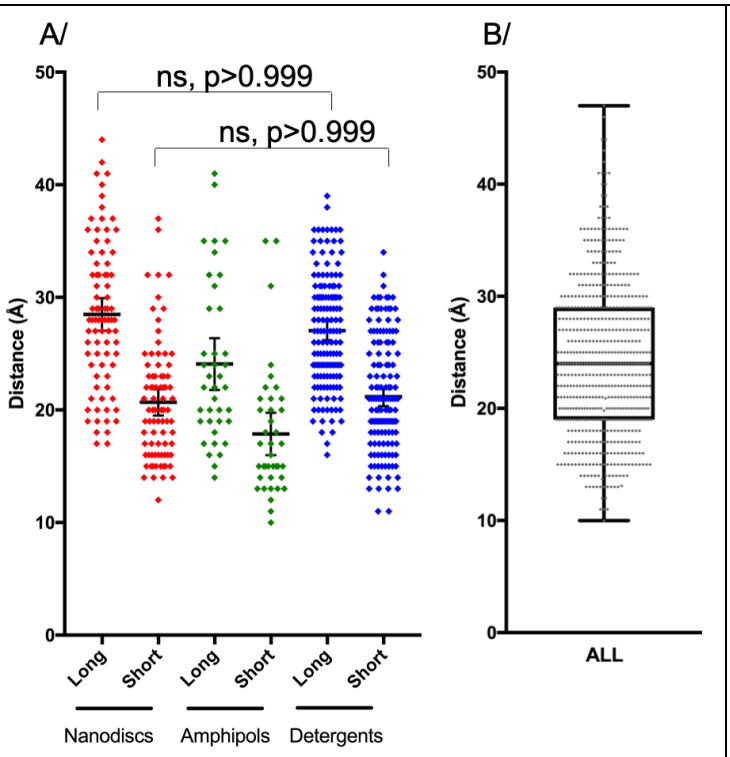

Fig. 2. Distance distributions between the protein edge and the belt boundary. **A/** Distances separeted by type of solvent. Nanodiscs (red), amphipols (green) and detergents (blue). Each dot corresponds to a distance, the horizontal bar is the mean with the error bar displaying the 95% confidence interval of the mean (reported in brackets bellow). Long and short distances are separated for clarity. Nanodiscs, long 28 Å [27-30] and short 21 Å [20-22]. Amphipols, long 24 Å [22-26] and short 18 Å [16-20]. Detergents, long 27 Å [26-28] and short 21 Å [20-22]. **B/** All distances represented by a grey dot. The box corresponds to the 25th (19 Å) and 75th (29 Å) percentile with an equal mean and median of 24 Å. 95% of total distances are comprised between 14 and 36 Å. P-values displayed are derived from an ANOVA test.

2.3. The TRPV family

The Transient Receptor Potential Vanilloid (TRPV) family consists of six ion channels, varying in ion-selectivity according to the sub-family. Despite being functionally distinct, they share a highly conserved fold, being active as a tetramer formed around 6 trans-membrane helices per monomer[24]. In the present dataset, we identified structures of TRPV1 in nanodiscs and amphipols, TRPV2 in nanodiscs, amphipols and detergents (LMNG and DMNG), TRPV3 in Nanodiscs, detergents and MSA-derived lipidic nanodiscs, and TRPV5 in nanodiscs and DMNG (STable 1.). The fact

that TRPV proteins share a conserved fold gives a unique opportunity to compare varying hydrophobic solvent belts. To these proteins, we also included structures of TRPV6 that were solved only in amphipols, benefiting from the fact that they share the same fold.

The signal of the hydrophobic belt varies in intensity among the different 3D reconstructions, for unclear reasons (Fig. 3A., SFig. 4-7.). For example, the nanodisc belt of TRPV1 and 2 appears with a strong signal in these five reconstructions, while its intensity is much milder in the two reconstructions of TRPV5. Similar trends can be seen in amphipols or detergents across the various reconstructions. Nevertheless, belt boundaries are clearly visible and were measured for all thirty proteins (Fig. 3BC.) Distance distributions follow a similar trend as the global one (Fig. 2A.), where differences amongst belts are undistinguishable. The same ambiguity remains between long distances of nanodiscs and amphipols, but it is challenged by the lack of difference this time between amphipols and detergents. More measures on more reconstructions would help to differentiate the trend. Nevertheless, the fact that short distances show the same distributions across the three types of solvent and the undistinguishable long distances for nanodiscs and detergents suggest a similar average size for solvent belts around TRPV proteins.

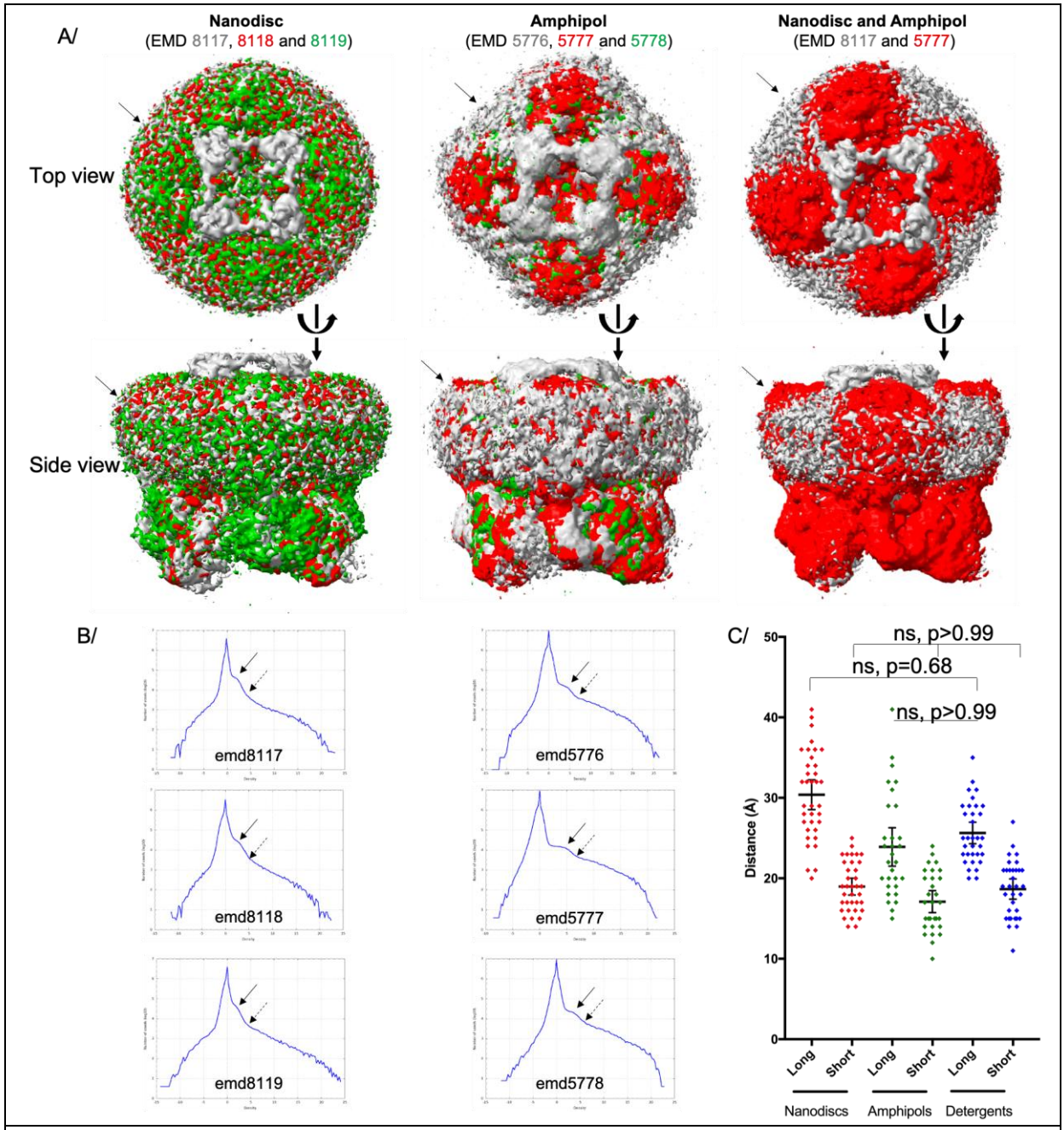

Fig. 3. Belts surrounding TRPV proteins. **A/** Example of the TRPV1 proteins solved in nanodisc or amphipols. The EMD accession codes are listed and each structure and are colored in grey, red or green, and overlaid. Top and side views are depicted, the solid arrow points to the position of the solvent belt. **B/** Map-density distribution for each entry. On each distribution, the dotted arrow shows the belt appearance at level 1, and the solid arrow at level 2. **C/** Distance distributions for all TRPV proteins, with the same color-coding as Fig.2. Statistical analysis was carried out using ANOVA and Kruskal-Wallis. Printed p-values are derived from Kruskal-Wallis analysis on ranks.

2.4. Similar average belts length across multiple protein types solved using different amphipathic solvents

We have identified in the dataset multiple protein structures that have been solved only a few times in different hydrophobic belts. This limited number of structures prevents a statistical analysis on each protein. Instead, these proteins were evaluated in a group, thereby offering the opportunity to compare proteins with completely distinct

folds, and originating from various sources and amphipathic environments (Fig. 4., STable 1., SFig. 8-13.). Within each protein, the hydrophobic belt distances cluster rather well, showing a narrow distribution of distances, sampling apparently randomly across the distribution of all proteins shown in Fig. 2. Comparison of all these proteins reveals that their means group in similar ranges, with overlapping confidence interval of the mean, invoking a comparable hydrophobic belt around all these proteins.

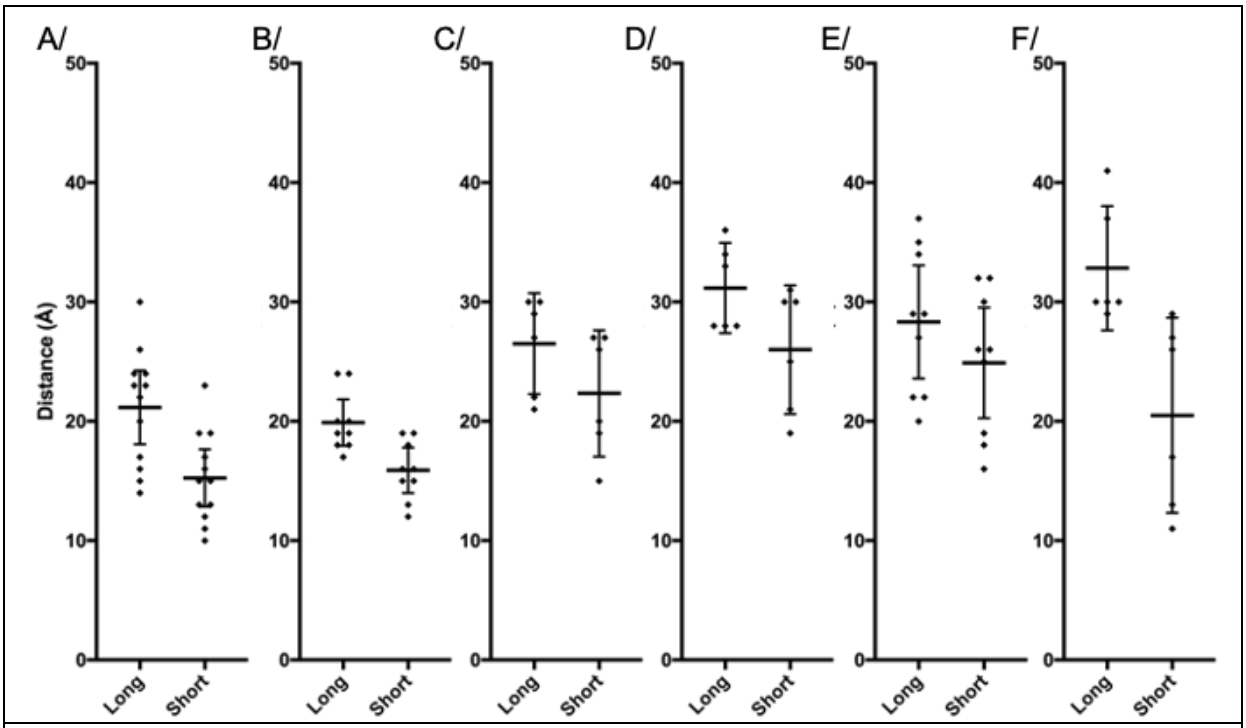

Fig. 4. Distance distributions between the protein edge and the belt boundary for several types of proteins. Given the limited number of structures in each family, nanodiscs, amphipols and detergents have been reported together. Each dot corresponds to a distance, the horizontal bar is the mean with the error bar displaying the 95% confidence interval of the mean (also in brackets below). Long and short distances are separated for clarity. **A/** PDK-TRP family, long 21 Å [18-24] and short 15 Å [13-18]. **B/** V-ATPase, long 20 Å [18-22] and short 16 Å [14-18]. **C/** OTP3, long 27 Å [22-31] and short 22 Å [17-28]. **D/** OSCA, long 31 Å [27-35] and short 26 Å [21-31]. **E/** LRRC8A, long 28 Å [24-33] and short 25 Å [20-30]. **F/** TMEM16, long 33 Å [28-38] and short 21 Å [12-29].

2.5. The superfamily of ABC transporters

ATP-binding Cassette (ABC) transporters are a large superfamily of transporters, harnessing the energy of ATP-binding and hydrolysis to translocate a wide range of substrate across many biological membranes. They are ubiquitous, and involved in many important cell-homeostasis functions[25]. While no single ABC transporter has been solved by cryo-EM in different hydrophobic environment, these proteins display a common fold and all together have been solved in nanodiscs, amphipols and detergents. They also offer the advantage that there is a large amount of structures, solved by several groups around the world using their own methodologies, and that their structures have been solved in multiple conformations offering a unique view of the solvent distribution around proteins in motion. Type I (or Type-V exporter, ABCB1-like) and type II (or Type-VI exporter, ABCG2-like) have been separated for clearer analysis (Fig. 5AB., SFig. 14-16.). Within the type I, no difference is detected between the distance distributions. Between type I and II, the distances are also inseparable, claiming that the

hydrophobic belt around ABC transporters is always of similar size, regardless of the conformation or the arrangement of trans-membrane helices.

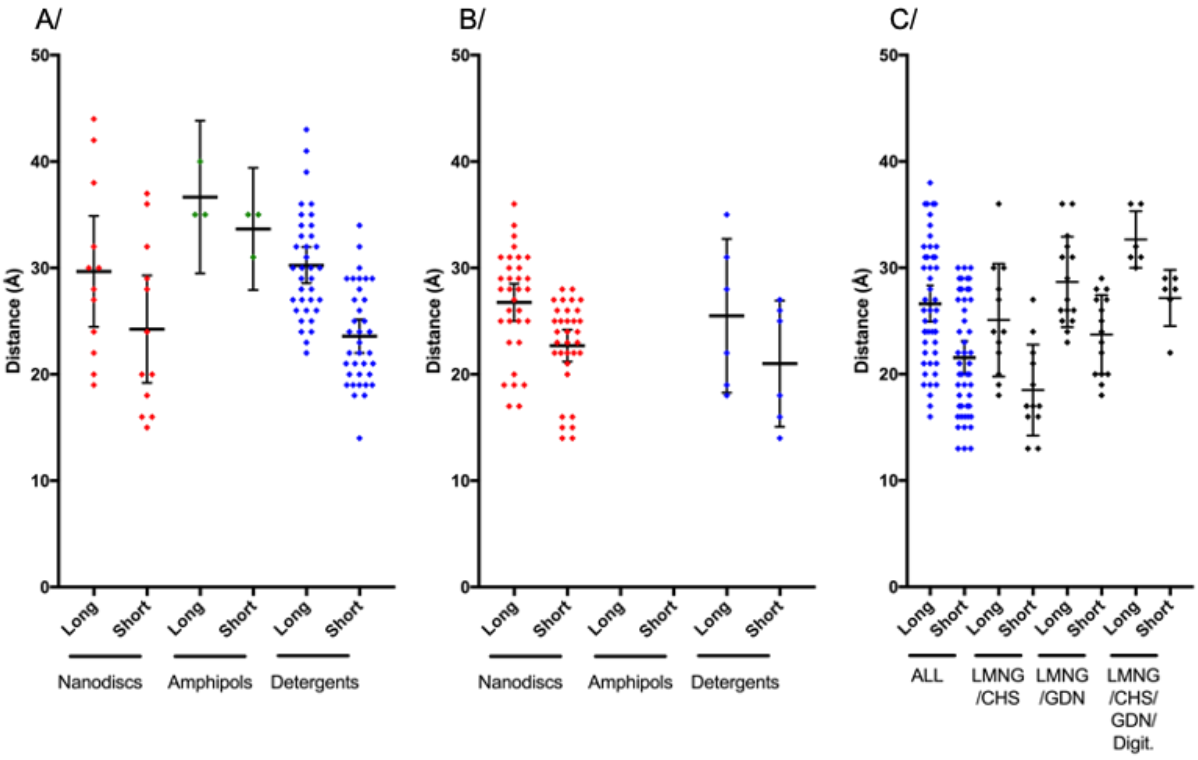

Fig. 5. Distance distributions around ABC transporters and GPCRs. **A/** Type V ABC transporter (ABCB1-like). Nanodiscs, long 30 Å [24-35] and short 25 Å [19-29]. Amphipols, long 37 Å [29-44] and short 34 Å [28-39]. Detergents, long 30 Å [29-32] and short 24 Å [22-25]. **B/** Type VI ABC transporter (ABCG2-like). Nanodiscs, long 27 Å [25-28] and short 23 Å [21-24]. Detergents, long 26 Å [18-33] and short 21 Å [15-27]. **C/** GPCR, all structures, in detergents: long 27 Å [25-28] and short 22 Å [20-23]. For structures solved in the mixture LMNG/CHS: long 25 Å [22-29] and short 19 Å [16-21]; LMNG/GDN: long 29 Å [26-31] and short 24 Å [22-26], and for the complex mixture of LMNG/CHS/GDN with or without digitonin: long 33 Å [30-36] and short 27 Å [24-30].

2.6. Similar detergent belt reconstructions around GPCRs

Twenty one unique structures of GPCR were found in the present database, belonging to the A, B, C or F classes (or G, R, F or S , respectively, according to the GRAFS nomenclature[26]), all solved in detergents. The vast majority used LMNG as a base, alone or in combination with other cholesterol-like detergents such as CHS, GDN or digitonin. All structures have been solved in complex with their cognate G proteins, and/or β-arrestin, in various flavors. Like for ABC transporters, all these GPCR structures share an overall fold that grants the direct comparison of their associated belts, with local differences between structures making it more worthwhile to analyze differences in the detergent belt measurements. The detergent belt distance distribution (Fig. 5., SFig. 17-18.) is inseparable from the ABC transporter ones, or from the global distance distribution of all membrane proteins solved by cryo-EM (Fig. 2.). Following this trend, the popular detergent mixes, for these GPCR structures, between LMNG and CHS, GDN or digitonin yield similar detergent belt reconstructions, on average.

2.7. Different types of nanodiscs yield similar reconstructions; detergent belts are all of equivalent sizes.

We checked whether a difference in distance distribution can be observed among the type of hydrophobic solvent. For instance, different flavors of Membrane Scaffold Proteins (MSP) are available to form nanodiscs, varying the length of a helical fragment within the MSP to make it longer or shorter[10]. In the current dataset, proteins have been solved with 3 types of MSP, the short MSP1D1 and its longest version MSP1E3D1 comprising 3 helical insertion. MSP2N2 is formed by the fusion of two MSP1D1. Figure 6A shows the distance distribution of the nanodisc belts sorted by nanodisc type, revealing that they are undistinguishable after reconstruction. Long and short distances of two types of nanodiscs formed by MSP1D1 and MSP2N2 follow the same distribution, with means equivalent to the mean obtained for all measurements in Fig. 2. Following this observation, distances were also separated by type of detergent to distinguish if a detergent or a detergent mixture can give rise to distinct belt sizes (Fig. 6B). Distances measured from different types of detergents are all virtually indissociable, and distribute in the same range as distances observed for nanodiscs and all other measurements together (Fig. 2.).

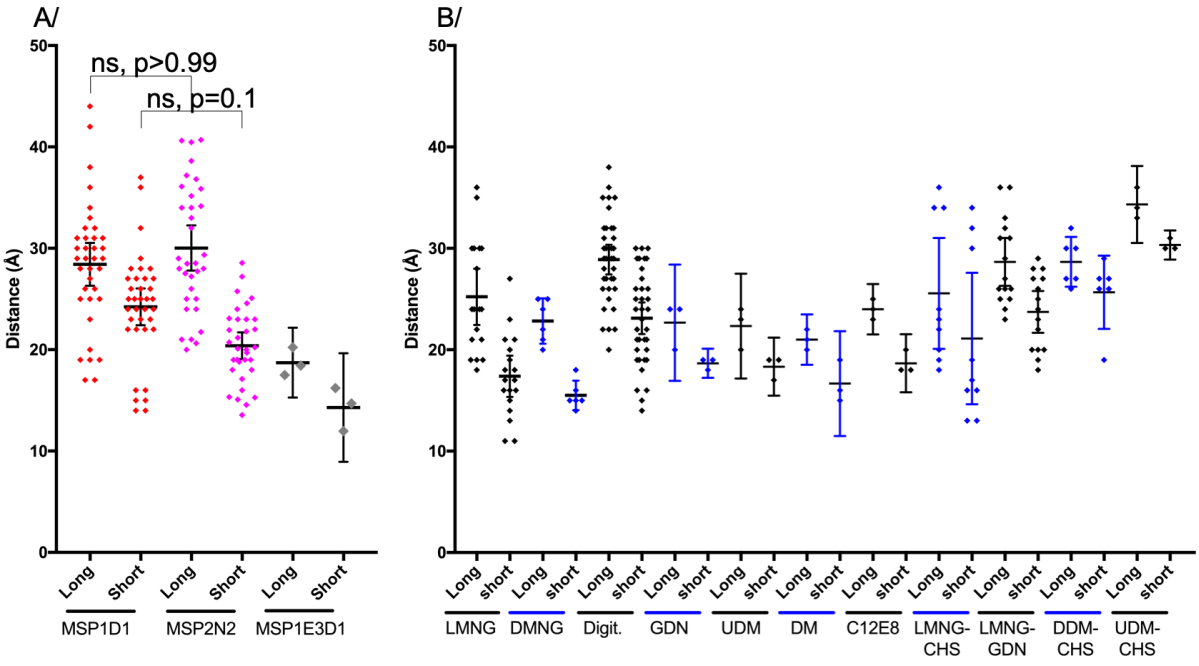

Fig. 6. Distance distributions of the different nanodiscs or detergents belts. **A/** Distances measured for nanodiscs belts. MSP1D1, long 28 Å [26-31] and short 24 Å [22-26]. MSP2N2, long 32 Å [30-35] and short 20 Å [18-22]. MSP1E3D1, long 19 Å [15-22] and short 14 Å [9-20]. **B/** Distances measured for the most represented detergents in this dataset. LMNG (Lauryl Maltose Neopentyl Glycol), long 25 Å [22-28] and short 17 Å [15-19]. DMNG (Decyl Maltose Neopentyl Glycol), long 23 Å [20-25] and short 16 Å [14-18]. Digit. (Digitonin), long 29 Å [27-30] and short 23 Å [22-25]. GDN (Glyco-diosgenin), long 23 Å [17-28] and short 19 Å [17-20]. UDM (Undecyl-β-D-galactopyranoside), long 22 Å [17-28] and short 18 Å [15-21]. DM (Decyl-β-D-galactopyranoside), long 21 Å [19-24] and short 17 Å [12-22]. C12E8 (Octaethylene Glycol Monododecyl Ether), long 24 Å [22-27] and short 19 Å [16-22]. LMNG-CHS (CHS: Cholesteryl-hemisuccinate), long 26 Å [20-31] and short 21 Å [15-28]. LMNG-GDN, long 29 Å [26-31] and short 24 Å [22-26]. DDM-CHS (DDM: Dodecyl-β-D-galactopyranoside), long 29 Å [26-31] and short 26 Å [22-29]. UDM-CHS, long 34 Å [31-38] and short 30 Å [29-32]. Numbers are the mean followed by the 95% confidence interval of the mean in brackets. Statistical analysis was carried out using ANOVA and Kruskal-Wallis. Printed p-values are derived from Kruskal-Wallis analysis on ranks.

3. Discussion

In order to discriminate if the compounds used to shield the membrane region of a membrane proteins have an influence on the observation of the corresponding belt by cryo-EM, we performed a statistical analysis of a curated database of selected membrane proteins solved in several hydrophobic environments. By visualizing every structure, we were able to identify in map-density distributions a signature of hydrophobic belt appearance (levels 1 & 2 in Fig. 1B.). We further identified its boundaries for every protein and measured its size for statistical analysis. 95% of all measured lengths distribute between 14 and 36 Å around the surface of trans-membrane segments, and half of the belts are comprised between 19 and 29 Å. Importantly, the distance distribution of amphipathic solvent belts varies significantly within the current data set, which is why the use of statistical tools to evaluate differences between populations is so important. We also only focused on protein from the same family to diminish the impact of proteins on reconstructions. It should be noted that the shape of the membrane protein, or the presence of a protein-protein complex, will have an influence on the reconstruction (which part of the particle dominate the reconstruction [23]), which will have an impact on the size of amphipathic belts, and can be seen as exceptions.

The hydrophobic belts were further separated by type of solvent to probe whether nanodiscs, amphipols or detergents can yield tighter or larger belts. The results presented in Figure 2 show that these three types of solvent were following the same distributions, and were therefore statistically indistinguishable on average.

This result correlates well with other types of measurements of the same solvents by other methods. Molecular dynamics simulations of membrane proteins embedded in amphipols or detergents show a belt around the transmembrane regions, with some degree of flexibility[4, 27-29]. Indeed, the belt formed by these amphipathic compounds is very fluid, revealing local clusters of individual molecules, forming and deforming with time. When measured using neutron diffraction of membrane protein crystals[30], an averaging technique like cryo-EM, the detergent belt appears as a homogeneous belt around the protein. The size of the belt observed was then highly dependent on the type of crystal as the detergent could merge between belts of symmetric molecules[31]. All these techniques have been limited to the size of the system for molecular dynamic simulations, or “neutron-diffraction quality” crystals combined with deuterated detergents; here, cryo-EM allows for the visualization of any amphipathic compound, with belt measurements matching other measuring methods.

Since the hydrophobic belt has intrinsic properties to diffract electrons, it has a strong influence on the reconstructions. For example, for a 130 kDa ABC transporter, the DDM belt (400 monomers) accounts for an additional 200 kDa[4]. It is thus understandable that even if this detergent belt is not ordered, it still influences electron diffraction around the membrane protein, nicely exemplified with 3D variability of the detergent belt visualized in cryo-EM[32].

Nanodiscs formation is achieved by mixing three ingredients (Membrane Scaffold Protein, lipids and membrane protein) and detergents removed using biobeads[10]. The membrane protein embedded into nanodiscs are then separated from empty nanodiscs using affinity chromatography and/or size exclusion chromatography. The object comprising the membrane protein of interest is in reality quite heterogeneous, containing a mixture of large and small nanodiscs, with more or less lipids embarked,

and varying in all dimensions according to the type of MSP used and the ratio lipid:MSP, etc... [33-36]. In some cases, contacts are made between the protein and the MSP that stabilize it and makes the MSP visible in 3D reconstruction, as exemplified recently[37, 38]. Most of the time however, the embarked membrane protein can move from side to side within the nanodisc, and does not always stay in the middle. The absence of a stable position makes it hard to visualize MSP positions by cryo-EM.

We next explored if we could identify within a set of protein, or type of amphipathic compound, a combination that could influence the size of the solvent belt seen around membrane proteins. We could not establish any significant difference in the measurement distributions, all falling within the overall distribution described in Figure 2. Hereabouts, the incorporation of ABC transporters and GPCRs in this dataset yields an important viewpoint. From detergent quantification we know that the amount of detergent present around membrane proteins is directly proportional to the accessible hydrophobic area[4]. The amount of detergent around ABC transporters (12 trans-membrane helices) is thus inherently larger than the one around GPCRs (7 trans-membrane helices). One would thus expect to visualize a larger belt around ABC transporters by cryo-EM, but the size of the belt is on the contrary following the same distribution (Fig. 5.).

Finally, there is the observation that the solvent belt observed around membrane proteins by cryo-EM is circular, somewhat reminiscent of the ones observed by neutron diffraction of crystals. This is partly due to symmetries enforced during reconstructions, but at the heart, mostly due to particle averaging. Particle alignments are anchored on secondary structures, among which trans-membrane helices are a lighthouse in a fog of amphipathic solvent. The solvent observed during reconstruction is thus made out of several layers distributing radially away from the protein boundary (Fig. 7.). Such behavior is enhanced when symmetry is applied, as can be seen on SFigures 4 or 6 for example, where the belt follow the protein edge exactly with sharp edges that are not physiological, but are the results of symmetry enforced reconstructions. The higher the symmetry, the more pronounced the effect will be on reconstructions of amphipathic belts. Level 1 corresponds to the highest density, and represents the common minimum ordered layer, where the amphipathic compound is always present around the membrane protein. This layer concomitantly increases in size and decreases in density as it radiates away from the protein boundary, representing areas of space less and less populated by the solvent. This is influenced by the fluid properties of the solvent, as the sample is vitrified in liquid ethane. Each individual particle of a dataset represents a snapshot carrying its own belt-distribution. These observations reinforce the idea that the belt visualized by cryo-EM is a fraction of the volume occupied by the hydrophobic belt and represents the common minimum ordered solvent surrounding the protein. The present study aims at bringing this awareness on the interpretation of biochemical data in the light of cryo-EM 3D reconstructions.

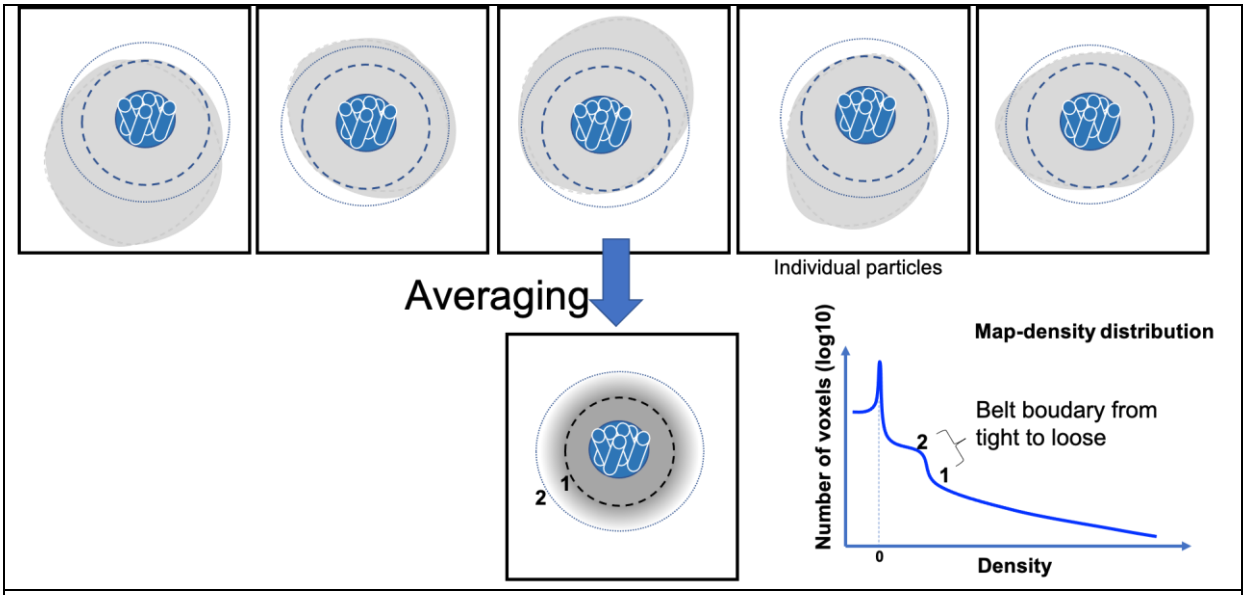

Fig. 7. Influence of the averaging on hydrophobic solvent visualization. Top: set of particles all centered on the trans-membrane helices, with the same orientation. The inner dash circle represents the volume around the membrane protein where the hydrophobic solvent is always present. The outer dotted circle represents the spread upto where the solvent belt can be visualized. The solvent is shown in gray, with various shapes to highlight its variability around the trans-membrane domain. Bottom: The result of the averaging is a clear definition of transmembrane helices, and a gradient of presence for the solvent radiating away from the protein boundary. The level 1 and 2 correspond to the levels presented on the map-density distribution.

4. Material and methods

4.1. Membrane proteins structure database extraction

Based on the mpstruc database (https://blanco.biomol.uci.edu/mpstruc/) that lists all the membrane proteins of known 3D structure, we created a dataset containing only entries solved by Cryo-EM, as of January 17th, 2020. We wrote a Bash shell script in order to automatically extract information from these entries. This allowed us to determine those which have been solved in multiple hydrophobic environments (nanodiscs, amphipols or detergents) and to sort them in distinct subsets. Then, for each entry, we extracted from the Electron Microscopy Data Bank (EMDB) the map-density distribution data in order to render graphs plotting the density distribution (*i.e.* the number of voxels as a function of the density).

In order to create the graph of membrane structure determination by method over the years, a local copy of the RCSB Protein Data Bank (PDB) was parsed over each entry to extract the REVDAT record giving us their deposition years, as well as the EXPDATA record identifying the experimental technique used to solve the structure. This dataset was crossed with the above mpstruct database. Data were then classified in four groups of techniques (X-ray diffraction, Cryo-EM, liquid NMR and solid-state NMR) and numbered according to the deposition year.

4.2. Map comparison

Maps were retrieved from EMDB and opened in ChimeraX[39]. Maps were first manually aligned, then aligned using the volume tool within ChimeraX. Threshold levels

to compare the maps were adjusted to include the highest level of low contour information (level 2 in Fig 1B), without including noise voxels appearing in the box.

4.3. Measures of the solvent belt around the protein

The measure of solvent belt thickness was performed in ChimeraX using the tool "tape" which is included in the software. The density map histogram was used to increase or decrease the contour information. Level 1 and 2 were manually chosen upon map and map-histogram inspection. At first, the density map showed the maximum of the solvent belt information (Level 2) and vertical lines were drawn to signal the limit the solvent belt. Then the density map contour was reduced in order to see clearly the protein density (Level 0). Horizontal lines were drawn to link the vertical lines and the protein density. The tape tool measured the distance (SFig. 2). This experiment was performed six times and in distinct positions of the solvent belt. Note that low-pass filtering of maps yields a clearer and sharper edge for the amphipathic belt, that could be useful for measurement. A major drawback of these maps is the absence of noise that makes it impossible to distinguish when to stop the map contour level, and would result in inconsistent measurements across the dataset (SFig 3). All measurements were therefore conducted on non-filtered maps.

All structures from which measurements were derived are listed in STable1 and measurements are presented in STable2. For example, 12 TRPV proteins in nanodiscs were included in the study, for which 3 measurements were carried out, making a total of 36 data points shown in Figure 3C.

4.4. Statistical analysis

Statistical analysis (Prism.v7.2) was performed only when the amount of measures was sufficient to perform meaningful statistics. For this reason, some measures in amphipols or on individual types of proteins or hydrophobic environments were excluded. ANOVA was used to distinguish differences between means, and Kruskal-Wallis was used to distinguish differences on ranks. For all figures, means were computed as well as the 95% confidence interval of the mean. Statistics are very useful to distinguish differences within distributions, especially when, as it is the case in this manuscript, data overlap. Statistics are thus used to differentiate whether distributions are undifferentiable or different. Parametric statistics compare distributions of means, and give confidence interval of the mean. These metrics are useful to interpret the data, but they are also skewed by the number of data points used. The larger the number, the better the definition of the distribution. Usually, 30 to 50 individual data points is considered a minimum for parametric statistics [40]. Non-parametric statistics differentiate distributions based on ranks and are less sensitive to the amount of data points and to outliers. Both statistical methods were used on the data sets evaluated. In case of a difference in significance, non-parametric statistics were preferred and reported.

Author contributions

XR extracted the database. VZ measured all distances. VZ, AG and VC created the figures and analysed the data. All authors wrote the manuscript.

Acknowledgments

This work was supported by the CNRS, Lyon University and the French National Research Agency, ANR-CLAMP2-18-CE11-0002-01 to PF and VC and ANR-19-CE11-0023-01 to VC and PF.

References

1. Choy, B.C., et al., *A 10-year meta-analysis of membrane protein structural biology: Detergents, membrane mimetics, and structure determination techniques.* Biochimica et Biophysica Acta (BBA) - Biomembranes, 2021. **1863**(3): p. 183533.
2. Le Bon, C., et al., *Amphipathic environments for determining the structure of membrane proteins by single-particle electron cryo-microscopy.* Q Rev Biophys, 2021: p. 1-62.
3. Seddon, A.M., P. Curnow, and P.J. Booth, *Membrane proteins, lipids and detergents: not just a soap opera.* Biochim Biophys Acta, 2004. **1666**(1-2): p. 105-17.
4. Chaptal, V., et al., *Quantification of Detergents Complexed with Membrane Proteins.* Sci Rep, 2017. **7**: p. 41751.
5. Chae, P.S., et al., *Maltose-neopentyl glycol (MNG) amphiphiles for solubilization, stabilization and crystallization of membrane proteins.* Nat Methods, 2010. **7**(12): p. 1003-8.
6. Lee, S.C., et al., *Steroid-based facial amphiphiles for stabilization and crystallization of membrane proteins.* Proc Natl Acad Sci U S A, 2013. **110**(13): p. E1203-11.
7. Lund, S., et al., *Detergent structure and associated lipid as determinants in the stabilization of solubilized Ca2+-ATPase from sarcoplasmic reticulum.* J Biol Chem, 1989. **264**(9): p. 4907-15.
8. Nguyen, K.A., et al., *Glycosyl-Substituted Dicarboxylates as Detergents for the Extraction, Overstabilization, and Crystallization of Membrane Proteins.* Angew Chem Int Ed Engl, 2018. **57**(11): p. 2948-2952.
9. Jiang, X., et al., *Evidence for an intermediate conformational state of LacY.* Proc Natl Acad Sci U S A, 2012.
10. Bayburt, T.H. and S.G. Sligar, *Membrane protein assembly into Nanodiscs.* FEBS Lett, 2010. **584**(9): p. 1721-7.
11. Oluwole, A.O., et al., *Solubilization of Membrane Proteins into Functional Lipid-Bilayer Nanodiscs Using a Diisobutylene/Maleic Acid Copolymer.* Angew Chem Int Ed Engl, 2017. **56**(7): p. 1919-1924.
12. Dörr, J.M., et al., *The styrene-maleic acid copolymer: a versatile tool in membrane research.* Eur Biophys J, 2016. **45**(1): p. 3-21.
13. Marconnet, A., et al., *Solubilization and Stabilization of Membrane Proteins by Cycloalkane-Modified Amphiphilic Polymers.* Biomacromolecules, 2020.
14. Salnikov, E.S., et al., *Solid-state NMR structural investigations of peptide-based nanodiscs and of transmembrane helices in bicellar arrangements.* Chemistry and Physics of Lipids, 2019. **219**: p. 58-71.
15. Overduin, M. and M. Esmaili, *Memtein: The fundamental unit of membrane-protein structure and function.* Chemistry and Physics of Lipids, 2019. **218**: p. 73-84.
16. Krishnarjuna, B., T. Ravula, and A. Ramamoorthy, *Detergent-free extraction, reconstitution and characterization of membrane-anchored cytochrome-b5 in native lipids.* Chemical Communications, 2020. **56**(48): p. 6511-6514.
17. Prade, E., et al., *A Minimal Functional Complex of Cytochrome P450 and FBD of Cytochrome P450 Reductase in Nanodiscs.* Angew Chem Int Ed Engl, 2018. **57**(28): p. 8458-8462.

18. Dufourc, E.J., *Bicelles and nanodiscs for biophysical chemistry.* Biochim Biophys Acta Biomembr, 2021. **1863**(1): p. 183478.
19. Ravula, T., N.Z. Hardin, and A. Ramamoorthy, *Polymer nanodiscs: Advantages and limitations.* Chemistry and Physics of Lipids, 2019. **219**: p. 45-49.
20. Johansen, N.T., et al., *Structural and Biophysical Properties of Supercharged and Circularized Nanodiscs.* Langmuir, 2021.
21. Bengtsen, T., et al., *Structure and dynamics of a nanodisc by integrating NMR, SAXS and SANS experiments with molecular dynamics simulations.* Elife, 2020. **9**.
22. Stepien, P., et al., *Complexity of seemingly simple lipid nanodiscs.* Biochim Biophys Acta Biomembr, 2020. **1862**(11): p. 183420.
23. Scheres, S.H.W., *Chapter Six - Processing of Structurally Heterogeneous Cryo-EM Data in RELION*, in *Methods in Enzymology*, R.A. Crowther, Editor. 2016, Academic Press. p. 125-157.
24. van Goor, M.K., et al., *High-resolution structures of transient receptor potential vanilloid channels: Unveiling a functionally diverse group of ion channels.* Protein Sci, 2020. **29**(7): p. 1569-1580.
25. Thomas, C. and R. Tampé, *Structural and Mechanistic Principles of ABC Transporters.* Annu Rev Biochem, 2020. **89**: p. 605-636.
26. Fredriksson, R., et al., *The G-Protein-Coupled Receptors in the Human Genome Form Five Main Families: Phylogenetic Analysis, Paralogon Groups, and Fingerprints.* Molecular Pharmacology, 2003. **63**(6): p. 1256-1256-1272.
27. Perlmutter, J.D., J.-L. Popot, and J.N. Sachs, *Molecular Dynamics Simulations of a Membrane Protein/Amphipol Complex.* The Journal of Membrane Biology, 2014. **247**(9): p. 883-895.
28. Etzkorn, M., et al., *How Amphipols Embed Membrane Proteins: Global Solvent Accessibility and Interaction with a Flexible Protein Terminus.* The Journal of Membrane Biology, 2014. **247**(9): p. 965-970.
29. Wolfe, A.J., et al., *Quantification of Membrane Protein-Detergent Complex Interactions.* The Journal of Physical Chemistry B, 2017. **121**(44): p. 10228-10241.
30. Pebay-Peyroula, E., et al., *Detergent structure in tetragonal crystals of OmpF porin.* Structure, 1995. **3**(10): p. 1051-9.
31. Penel, S., et al., *Detergent binding in trigonal crystals of OmpF porin from Escherichia coli.* Biochimie, 1998. **80**(5-6): p. 543-51.
32. Punjani, A. and D.J. Fleet, *3D Variability Analysis: Directly resolving continuous flexibility and discrete heterogeneity from single particle cryo-EM images.* bioRxiv, 2020: p. 2020.04.08.032466.
33. Harvey, S.R., et al., *Probing the structure of nanodiscs using surface-induced dissociation mass spectrometry.* Chem Commun (Camb), 2020. **56**(100): p. 15651-15654.
34. Reis, R.I. and I. Moraes, *Probing Membrane Protein Assembly into Nanodiscs by In Situ Dynamic Light Scattering: A(2A) Receptor as a Case Study.* Biology (Basel), 2020. **9**(11).
35. Denisov, I.G. and S.G. Sligar, *Nanodiscs in Membrane Biochemistry and Biophysics.* Chemical Reviews, 2017. **117**(6): p. 4669-4713.
36. Inagaki, S., R. Ghirlando, and R. Grisshammer, *Biophysical characterization of membrane proteins in nanodiscs.* Methods, 2013. **59**(3): p. 287-300.
37. Chen, I., et al., *Glutamate transporters have a chloride channel with two hydrophobic gates.* Nature, 2021.

38. Kern, D.M., et al., *Cryo-EM structure of the SARS-CoV-2 3a ion channel in lipid nanodiscs.* bioRxiv, 2021: p. 2020.06.17.156554.
39. Goddard, T.D., et al., *UCSF ChimeraX: Meeting modern challenges in visualization and analysis.* Protein Sci, 2018. **27**(1): p. 14-25.
40. Student, *The Probable Error of a Mean.* Biometrika, 1908. **6**(1): p. 1-25.
41. Liao, M., et al., *Structure of the TRPV1 ion channel determined by electron cryo-microscopy.* Nature, 2013. **504**(7478): p. 107-12.
42. Cao, E., et al., *TRPV1 structures in distinct conformations reveal activation mechanisms.* Nature, 2013. **504**(7478): p. 113-8.
43. Gao, Y., et al., *TRPV1 structures in nanodiscs reveal mechanisms of ligand and lipid action.* Nature, 2016. **534**(7607): p. 347-51.
44. Pumroy, R.A., et al., *Molecular mechanism of TRPV2 channel modulation by cannabidiol.* Elife, 2019. **8**.
45. Zubcevic, L., et al., *Cryo-electron microscopy structure of the TRPV2 ion channel.* Nat Struct Mol Biol, 2016. **23**(2): p. 180-186.
46. Zubcevic, L., et al., *Symmetry transitions during gating of the TRPV2 ion channel in lipid membranes.* Elife, 2019. **8**.
47. Dosey, T.L., et al., *Structures of TRPV2 in distinct conformations provide insight into role of the pore turret.* Nat Struct Mol Biol, 2019. **26**(1): p. 40-49.
48. Huynh, K.W., et al., *Structure of the full-length TRPV2 channel by cryo-EM.* Nat Commun, 2016. **7**: p. 11130.
49. Singh, A.K., L.L. McGoldrick, and A.I. Sobolevsky, *Structure and gating mechanism of the transient receptor potential channel TRPV3.* Nat Struct Mol Biol, 2018. **25**(9): p. 805-813.
50. Shimada, H., et al., *The structure of lipid nanodisc-reconstituted TRPV3 reveals the gating mechanism.* Nat Struct Mol Biol, 2020. **27**(7): p. 645-652.
51. Zubcevic, L., et al., *Conformational ensemble of the human TRPV3 ion channel.* Nat Commun, 2018. **9**(1): p. 4773.
52. Deng, Z., et al., *Gating of human TRPV3 in a lipid bilayer.* Nat Struct Mol Biol, 2020. **27**(7): p. 635-644.
53. Singh, A.K., et al., *Structural basis of temperature sensation by the TRP channel TRPV3.* Nat Struct Mol Biol, 2019. **26**(11): p. 994-998.
54. Hughes, T.E., et al., *Structure-based characterization of novel TRPV5 inhibitors.* Elife, 2019. **8**.
55. Dang, S., et al., *Structural insight into TRPV5 channel function and modulation.* Proc Natl Acad Sci U S A, 2019. **116**(18): p. 8869-8878.
56. Singh, A.K., et al., *Structural bases of TRP channel TRPV6 allosteric modulation by 2-APB.* Nat Commun, 2018. **9**(1): p. 2465.
57. Kasuya, G., et al., *Cryo-EM structures of the human volume-regulated anion channel LRRC8.* Nat Struct Mol Biol, 2018. **25**(9): p. 797-804.
58. Kern, D.M., et al., *Cryo-EM structures of the DCPIB-inhibited volume-regulated anion channel LRRC8A in lipid nanodiscs.* Elife, 2019. **8**.
59. Kefauver, J.M., et al., *Structure of the human volume regulated anion channel.* Elife, 2018. **7**.
60. Dang, S., et al., *Cryo-EM structures of the TMEM16A calcium-activated chloride channel.* Nature, 2017. **552**(7685): p. 426-429.
61. Mazhab-Jafari, M.T., et al., *Atomic model for the membrane-embedded V(O) motor of a eukaryotic V-ATPase.* Nature, 2016. **539**(7627): p. 118-122.

62. Roh, S.H., et al., *The 3.5-Å CryoEM Structure of Nanodisc-Reconstituted Yeast Vacuolar ATPase V(o) Proton Channel.* Mol Cell, 2018. **69**(6): p. 993-1004.e3.
63. Vasanthakumar, T., et al., *Structural comparison of the vacuolar and Golgi V-ATPases from Saccharomyces cerevisiae.* Proc Natl Acad Sci U S A, 2019. **116**(15): p. 7272-7277.
64. Saotome, K., et al., *Structures of the otopetrin proton channels Otop1 and Otop3.* Nat Struct Mol Biol, 2019. **26**(6): p. 518-525.
65. Chen, Q., et al., *Structural and functional characterization of an otopetrin family proton channel.* Elife, 2019. **8**.
66. Jojoa-Cruz, S., et al., *Cryo-EM structure of the mechanically activated ion channel OSCA1.2.* Elife, 2018. **7**.
67. Maity, K., et al., *Cryo-EM structure of OSCA1.2 from Oryza sativa elucidates the mechanical basis of potential membrane hyperosmolality gating.* Proc Natl Acad Sci U S A, 2019. **116**(28): p. 14309-14318.
68. Shen, P.S., et al., *The Structure of the Polycystic Kidney Disease Channel PKD2 in Lipid Nanodiscs.* Cell, 2016. **167**(3): p. 763-773.e11.
69. Su, Q., et al., *Structure of the human PKD1-PKD2 complex.* Science, 2018. **361**(6406).
70. Grieben, M., et al., *Structure of the polycystic kidney disease TRP channel Polycystin-2 (PC2).* Nat Struct Mol Biol, 2017. **24**(2): p. 114-122.
71. Wilkes, M., et al., *Molecular insights into lipid-assisted Ca(2+) regulation of the TRP channel Polycystin-2.* Nat Struct Mol Biol, 2017. **24**(2): p. 123-130.
72. Mi, W., et al., *Structural basis of MsbA-mediated lipopolysaccharide transport.* Nature, 2017. **549**(7671): p. 233-237.
73. Chaptal, V., et al., *Drug-bound and -free outward-facing structures of a multidrug ABC exporter point to a swing mechanism.* bioRxiv, 2021: p. 2021.03.12.435132.
74. Alam, A., et al., *Structural insight into substrate and inhibitor discrimination by human P-glycoprotein.* Science, 2019. **363**(6428): p. 753-756.
75. Kim, Y. and J. Chen, *Molecular structure of human P-glycoprotein in the ATP-bound, outward-facing conformation.* Science, 2018. **359**(6378): p. 915-919.
76. Alam, A., et al., *Structure of a zosuquidar and UIC2-bound human-mouse chimeric ABCB1.* Proc Natl Acad Sci U S A, 2018. **115**(9): p. E1973-e1982.
77. Fay, J.F., et al., *Cryo-EM Visualization of an Active High Open Probability CFTR Anion Channel.* Biochemistry, 2018. **57**(43): p. 6234-6246.
78. Zhang, Z., F. Liu, and J. Chen, *Molecular structure of the ATP-bound, phosphorylated human CFTR.* Proc Natl Acad Sci U S A, 2018. **115**(50): p. 12757-12762.
79. Liu, F., et al., *Molecular Structure of the Human CFTR Ion Channel.* Cell, 2017. **169**(1): p. 85-95.e8.
80. Zhang, Z. and J. Chen, *Atomic Structure of the Cystic Fibrosis Transmembrane Conductance Regulator.* Cell, 2016. **167**(6): p. 1586-1597.e9.
81. Liu, F., et al., *Structural identification of a hotspot on CFTR for potentiation.* Science, 2019. **364**(6446): p. 1184-1188.
82. Zhang, Z., F. Liu, and J. Chen, *Conformational Changes of CFTR upon Phosphorylation and ATP Binding.* Cell, 2017. **170**(3): p. 483-491.e8.
83. Johnson, Z.L. and J. Chen, *Structural Basis of Substrate Recognition by the Multidrug Resistance Protein MRP1.* Cell, 2017. **168**(6): p. 1075-1085.e9.
84. Johnson, Z.L. and J. Chen, *ATP Binding Enables Substrate Release from Multidrug Resistance Protein 1.* Cell, 2018. **172**(1-2): p. 81-89.e10.

85. Oldham, M.L., N. Grigorieff, and J. Chen, *Structure of the transporter associated with antigen processing trapped by herpes simplex virus.* Elife, 2016. **5**.
86. Taylor, N.M.I., et al., *Structure of the human multidrug transporter ABCG2.* Nature, 2017. **546**(7659): p. 504-509.
87. Jackson, S.M., et al., *Structural basis of small-molecule inhibition of human multidrug transporter ABCG2.* Nat Struct Mol Biol, 2018. **25**(4): p. 333-340.
88. Manolaridis, I., et al., *Cryo-EM structures of a human ABCG2 mutant trapped in ATP-bound and substrate-bound states.* Nature, 2018. **563**(7731): p. 426-430.
89. Qian, H., et al., *Structure of the Human Lipid Exporter ABCA1.* Cell, 2017. **169**(7): p. 1228-1239.e10.
90. Li, Y., B.J. Orlando, and M. Liao, *Structural basis of lipopolysaccharide extraction by the LptB(2)FGC complex.* Nature, 2019. **567**(7749): p. 486-490.
91. Tang, X., et al., *Cryo-EM structures of lipopolysaccharide transporter LptB(2)FGC in lipopolysaccharide or AMP-PNP-bound states reveal its transport mechanism.* Nat Commun, 2019. **10**(1): p. 4175.
92. Liang, Y.L., et al., *Phase-plate cryo-EM structure of a class B GPCR-G-protein complex.* Nature, 2017. **546**(7656): p. 118-123.
93. Liang, Y.-L., et al., *Cryo-EM structure of the active, Gs-protein complexed, human CGRP receptor.* Nature, 2018. **561**(7724): p. 492-497.
94. Kang, Y., et al., *Cryo-EM structure of human rhodopsin bound to an inhibitory G protein.* Nature, 2018. **558**(7711): p. 553-558.
95. Draper-Joyce, C.J., et al., *Structure of the adenosine-bound human adenosine A(1) receptor-G(i) complex.* Nature, 2018. **558**(7711): p. 559-563.
96. Liang, Y.L., et al., *Phase-plate cryo-EM structure of a biased agonist-bound human GLP-1 receptor-Gs complex.* Nature, 2018. **555**(7694): p. 121-125.
97. García-Nafría, J., et al., *Cryo-EM structure of the serotonin 5-HT(1B) receptor coupled to heterotrimeric G(o).* Nature, 2018. **558**(7711): p. 620-623.
98. García-Nafría, J., et al., *Cryo-EM structure of the adenosine A(2A) receptor coupled to an engineered heterotrimeric G protein.* Elife, 2018. **7**.
99. Krishna Kumar, K., et al., *Structure of a Signaling Cannabinoid Receptor 1-G Protein Complex.* Cell, 2019. **176**(3): p. 448-458.e12.
100. Zhao, L.H., et al., *Structure and dynamics of the active human parathyroid hormone receptor-1.* Science, 2019. **364**(6436): p. 148-153.
101. Nguyen, A.H., et al., *Structure of an endosomal signaling GPCR-G protein-β-arrestin megacomplex.* Nat Struct Mol Biol, 2019. **26**(12): p. 1123-1131.
102. Maeda, S., et al., *Structures of the M1 and M2 muscarinic acetylcholine receptor/G-protein complexes.* Science, 2019. **364**(6440): p. 552-557.
103. Kato, H.E., et al., *Conformational transitions of a neurotensin receptor 1-G(i1) complex.* Nature, 2019. **572**(7767): p. 80-85.
104. Qi, X., et al., *Cryo-EM structure of oxysterol-bound human Smoothened coupled to a heterotrimeric G(i).* Nature, 2019. **571**(7764): p. 279-283.
105. Gao, Y., et al., *Structures of the Rhodopsin-Transducin Complex: Insights into G-Protein Activation.* Mol Cell, 2019. **75**(4): p. 781-790.e3.
106. Yin, W., et al., *A complex structure of arrestin-2 bound to a G protein-coupled receptor.* Cell Res, 2019. **29**(12): p. 971-983.
107. Tsai, C.J., et al., *Cryo-EM structure of the rhodopsin-Gαi-βγ complex reveals binding of the rhodopsin C-terminal tail to the gβ subunit.* Elife, 2019. **8**.

STable 1: List of proteins included in the study. The table relates for each protein the Protein Data Bank (PDB) entry, the Electron Microscopy Database (EMD) entry, the release year, the symmetry employed, the overall resolution, the nature of the amphipathic compound used to solve the structure (final purification step), and the reference of the structure. (-) means that the information was unavailable or not clearly retrievable.

PROTEIN	PDB	EMD	YEAR	SYM.	RES. (Å)	Amphipathic compound	Reference
TRPV1	3J5P	5778	2013	C4	3.3	Amphipol	[41]
	3J5Q	5776	2013	C4	3.8	Amphipol	[42]
	3J5R	5777	2013	C4	4.2	Amphipol	[20]
	5IRX	8117	2016	C4	2.95	Nanodisc (MSP2N2)	[43]
	5IRZ	8118	2016	C4	3.28	Nanodisc (MSP2N2)	[43]
	5IS0	8119	2016	C4	3.4	Nanodisc (MSP2N2)	[43]
TRPV2	6U84	20677	2019	C4	3.7	Nanodisc (MSP2N2)	[44]
	5AN8	6455	2015	C4	3.8	Amphipol	[45]
	6OO3	20143	2019	C4	2.9	Nanodisc (MSP2N2)	[46]
	6BO4	7118	2018	C4	4.0	LMNG	[47]
	5HI9	6580	2016	C4	4.4	DMNG	[48]
TRPV3	6DVW	8919	2018	C4	4.3	Digitonin	[49]
	6DVY	8920	2018	C4	4.0	Digitonin	[49]
	6DVZ	8921	2018	C4	4.24	GDN	[49]
	6LGP	882	2019	C4	3.3	Nanodisc (MSP2N2)	[50]
	6MHO	9115	2018	C4	3.4	Poly (Maleic Anhydride-alt-1-Decene)/PMALC8	[51]
	6UW4	20917	2020	C4	3.1	Nanodisc (MSP2N2)	[52]
	6MHS	9117	2018	C4	3.2	Poly (Maleic Anhydride-alt-1-Decene)/PMALC8	[51]
	6UW6	20918	2020	C4	3.66	Nanodisc (MSP2N2)	[52]
	6UW9	20920	2020	C4	4.33	Nanodisc (MSP2N2)	[52]
	6UW8	20919	2020	C4	4.02	Nanodisc (MSP2N2)	[52]
	6PVL	20492	2019	C4	4.4	GDN	[53]
	6PVM	20493	2019	C4	4.5	GDN	[53]
	6PVO	20495	2019	C4	5.18	GDN	[53]
	6PVN	20494	2019	C4	4.07	GDN	[53]
	6PVP	20496	2019	C4	4.48	GDN	[53]
TRPV5	6B5V	7058	2017	C4	4.8	DMNG	[54]
	6O1N	593	2019	C4	2.9	Nanodisc (MSP2N2)	[55]
	6PBF	20292	2019	C4	4.2	Nanodisc (MSP2N2)	[54]
TRPV6	6D7T	7825	2018	C4	4.44	Amphipol	[56]
	6E2F	8961	2018	C1	3.9	Amphipol	[56]
	6E2G	8962	2018	C1	3.6	Amphipol	[56]
LRRC8A	5ZSU	6952	2018	C3	4.25	Digitonin	[57]
	6O00	564	2019	C6	4.18	Nanodisc (MSP1E3D1)	[58]
	6DJB	7935	2018	C3	4.4	Digitonin	[59]
TMEM16	6BGI	7095	2017	C2	3.8	Nanodisc (MSP2N2)	[60]
	6BGJ	7096	2017	C2	3.8	LMNG	[60]
V-ATPase	5TJ5	8409	2016	C1	3.9	Amphipol	[61]
	6C6L	7348	2018	C1	3.5	Nanodisc (MSP1E3D1)	[62]
	6O7T	644	2019	C1	3.2	GDN	[63]
OTP3	6NF6	9361	2019	C2	3.3	Nanodisc (MSP2N2)	[64]
	6O84	650	2019	-	3.92	DDM CHS	[65]
OSCA	6MGV	9112	2018	C2	3.1	Nanodisc (MSP2N2)	[66]
	6OCE	20017	2019	C2	4.9	UDM-CHS	[67]

PKD TRP	5T4D	8354	2016	-	3.0	Nanodisc	[68]
	6A70	6991	2018	-	3.6	Digitonin	[69]
	5K47	8200	2016	-	4.2	UDM	[70]
	5MKF	3524	2017	-	4.2	Amphipol	[71]
	5MKE	3523	2017	-	4.3	Amphipol	[71]
MsbA	5TTP	8467	2017	C2	4.8	Nanodisc (MSP1D1)	[72]
	5TV4	8469	2017	C1	4.2	Nanodisc (MSP1D1)	[72]
BmrA	6R81	4749	2020	C2	3.9	DDM-Cholate	[73]
Pgp	6QEE	4536	2019	C1	3.9	Nanodisc (MSP1D1)	[74]
	6C0V	7325	2018	C1	3.4	DDM-CHS	[75]
	6FN1	4281	2018	C1	3.58	Amphipol	[76]
	6FN4	4282	2018	C1	4.14	LMNG-CHS	[76]
	6QEX	4539	2019	-	3.6	Nanodisc (MSP1D1)	[74]
CFTR	6D3R	7793	2018	C2	4.30	Digitonin	[77]
	6MSM	9230	2018	-	3.20	Digitonin	[78]
	5UAK	8516	2017	-	3.87	Digitonin	[79]
	5UAR	8461	2016	-	3.73	-	[80]
	6O2P	0611	2019	-	3.3	-	[81]
	5W81	8782	2017	-	3.37	LMNG	[82]
MRP1	5UJ9	8559	2017	-	3.49	Digitonin	[83]
	5AUJ	8560	2017	-	3.34	Digitonin	[83]
	6BHU	7099	2017	-	3.14	Digitonin	[84]
TAP1/TAP2	5UJ9	8482	2017	-	3.97	C12E8	[85]
ABCG2	5NJG	3654	2017	-	3.78	Nanodisc (MSP1D1)	[86]
	6ETI	3953	2018	-	3.1	Nanodisc (MSP1D1)	[87]
	6FEQ	4246	2018	-	3.6	Nanodisc (MSP1D1)	[87]
	6FFC	4256	2018	C2	3.56	Nanodisc (MSP1D1)	[87]
	6HCO	0196	2018	C2	3.58	Nanodisc (MSP1D1)	[88]
	6HZM	0190	2018	C2	3.09	Nanodisc (MSP1D1)	[88]
ABCA1	5XJY	6724	2017	C1	4.10	Digitonin	[89]
LptB2FGC	6MI7	9125	2019	C1	4.2	Nanodisc (MSP1D1)	[90]
	6S8N	10125	2019	C1	3.10	LMNG	[91]
GPCR	5UZ7	8623	2017	C1	4.1	MNG/CHS	[92]
	6B3J	7039	2018	C1	3.3	MNG/CHS	[93]
	6CMO	7517	2018	C1	4.5	Digitonin	[94]
	6D9H	7835	2018	C1	3.6	LMNG/CHS	[95]
	6E3Y	8978	2018	C1	3.3	LMNG/CHS	[96]
	6G79	4358	2018	C1	3.78	DM	[97, 98]
	6N4B	0339	2019	C1	3	LMNG/GDN	[99]
	6NBF	0410	2019	C1	3	LMNG/GDN/CHS	[100]
	6NI3	9376	2019	C1	3,8	LMNG	[101]
	6OIJ	20078	2019	C1	3,3	LMNG/GDN	[102]
	6OIK	20079	2019	C1	3,6	LMNG/GDN	[79]
	6OS9	20180	2019	C1	3	LMNG/GDN	[103]
	6OT0	20190	2019	C1	3,84	MNG/GDN/ CHS/ Digitonin	[104]
	6OY9	20222	2019	C1	3,9	LMNG	[105]
	6PWC	20505	2019	C1	4,9	Digitonin	[106]
	6QNO	4598	2019	C1	4,38	-	[107]

1
2

STable2: Belt measurements for all entries listed in STable 1. For each entry, six measurements were performed in distinct positions of the solvent belt. Since heterogeneity in distances were clearly visible on each construction, the measurements were divided on long and short distances.

PROTEIN	PDB	EMD	SYM.	RES. (Å)	Amphipathic compound	Belt measurements (Å)					
						Long distances			Short distances		
TRPV1	3J5P	5778	C4	3.3	Amphipol	22	20	16	15	14	14
	3J5Q	5776	C4	3.8	Amphipol	25	24	23	22	21	20
	3J5R	5777	C4	4.2	Amphipol	29	22	24	21	19	18
	5IRX	8117	C4	2.95	Nanodisc (MSP2N2)	33	29	28	16	15	15
	5IRZ	8118	C4	3.28	Nanodisc (MSP2N2)	36	32	32	17	17	14
	5IS0	8119	C4	3.4	Nanodisc (MSP2N2)	36	32	32	19	18	17
TRPV2	6U84	20677	C4	3.7	Nanodisc (MSP2N2)	40	41	36	20	23	22
	5AN8	6455	C4	3.8	Amphipol	29	29	27	17	16	16
	6OO3	20143	C4	2.9	Nanodisc (MSP2N2)	34	32	29	20	15	15
	6BO4	7118	C4	4.0	LMNG	28	24	21	21	15	11
	5HI9	6580	C4	4.4	DMNG	24	25	22	15	15	14
TRPV3	6DVW	8919	C4	4.3	Digitonin	28	23	22	21	19	17
	6DVY	8920	C4	4.0	Digitonin	29	25	20	19	15	14
	6DVZ	8921	C4	4.24	GDN	28	27	25	24	23	21
	6LGP	882	C4	3.3	Nanodisc (MSP2N2)	32	27	26	21	23	19
	6MHO	9115	C4	3.4	Poly (Maleic Anhydride-alt-1-Decene)/PMALC8	35	32	25	23	21	17
	6UW4	20917	C4	3.1	Nanodisc (MSP2N2)	25	21	20	19	18	16
	6MHS	9117	C4	3.2	Poly (Maleic Anhydride-alt-1-Decene)/PMALC8	24	20	19	18	17	15
	6UW6	20918	C4	3.66	Nanodisc (MSP2N2)	34	33	28	24	23	22
	6UW9	20920	C4	4.33	Nanodisc (MSP2N2)	28	24	21	20	19	18
	6UW8	20919	C4	4.02	Nanodisc (MSP2N2)	26	25	24	23	23	19
	6PVL	20492	C4	4.4	GDN	25	23	23	22	21	16
	6PVM	20493	C4	4.5	GDN	32	30	29	27	23	18
	6PVO	20495	C4	5.18	GDN	29	23	22	21	20	19
	6PVN	20494	C4	4.07	GDN	31	24	23	21	18	15
	6PVP	20496	C4	4.48	GDN	35	31	29	22	21	19
TRPV5	6B5V	7058	C4	4.8	DMNG	25	21	20	18	16	15
	6O1N	593	C4	2.9	Nanodisc (MSP2N2)	35	34	27	17	15	14
	6PBF	20292	C4	4.2	Nanodisc (MSP2N2)	37	39	36	25	22	21
TRPV6	6D7T	7825	C4	4.44	Amphipol	20	19	17	15	15	13
	6E2F	8961	C1	3.9	Amphipol	41	31	25	24	22	20
	6E2G	8962	C1	3.6	Amphipol	21	20	18	17	14	13
LRRC8A	5ZSU	6952	C3	4.25	Digitonin	29	29	27	26	26	25
	6O00	564	C6	4.18	Nanodisc (MSP1E3D1)	37	34	35	32	32	30

	6DJB	7935	C3	4.4	Digitonin	22	22	20	19	18	16
TMEM16	6BGI	7095	C2	3.8	Nanodisc (MSP2N2)	41	37	29	29	27	26
	6BGJ	7096	C2	3.8	LMNG	30	30	30	17	13	11
V-ATPase	5TJ5	8409	C1	3.9	Amphipol	19	19	17	16	15	13
	6C6L	7348	C1	3.5	Nanodisc (MSP1E3D1)	20	18	18	16	15	12
	6O7T	644	C1	3.2	GDN	24	24	20	19	19	18
OTP3	6NF6	9361	C2	3.3	Nanodisc (MSP2N2)	29	22	21	20	19	15
	6O84	650	-	3.92	DDM CHS	30	30	27	27	27	26
OSCA	6MGV	9112	C2	3.1	Nanodisc (MSP2N2)	28	28	28	25	21	19
	6OCE	20017	C2	4.9	UDM-CHS	36	34	33	31	30	30
PKD TRP	5T4D	8354	-	3.0	Nanodisc	30	26	24	23	16	15
	6A70	6991	-	3.6	Digitonin	24	23	20	19	19	17
	5K47	8200	-	4.2	UDM	23	22	16	15	12	11
	5MKF	3524	-	4.2	Amphipol	17	15	14	13	13	10
	5MKE	3523	-	4.3	Amphipol	30	26	24	23	16	15
MsbA	5TTP	8467	C2	4.8	Nanodisc (MSP1D1)	28	24	22	20	20	16
	5TV4	8469	C1	4.2	Nanodisc (MSP1D1)	27	20	19	18	16	15
BmrA	6R81	4749	C2	3.9	DDM-Cholate	21	20	14	14	13	13
Pgp	6QEE	4536	C1	3.9	Nanodisc (MSP1D1)	44	42	38	37	36	32
	6C0V	7325	C1	3.4	DDM-CHS	32	27	26	29	19	26
	6FN1	4281	C1	3.58	Amphipol	40	35	35	35	35	31
	6FN4	4282	C1	4.14	LMNG-CHS	36	34	34	34	32	30
	6QEX	4539	-	3.6	Nanodisc (MSP1D1)	32	30	30	29	28	24
CFTR	6D3R	7793	C2	4.30	Digitonin	30	28	27	25	19	19
	6MSM	9230	-	3.20	Digitonin	35	31	30	29	29	24
	5UAK	8516	-	3.87	Digitonin	32	30	29	24	21	21
	5UAR	8461	-	3.73	-	43	41	33	29	28	25
	6O2P	0611	-	3.3	-	39	33	28	29	27	22
	5W81	8782	-	3.37	LMNG	36	35	30	27	23	19
MRP1	5UJ9	8559	-	3.49	Digitonin	32	27	26	24	22	22
	5AUJ	8560	-	3.34	Digitonin	29	25	22	20	20	19
	6BHU	7099	-	3.14	Digitonin	27	26	24	21	21	14
TAP1/TAP2	5UJ9	8482	-	3.97	C12E8	25	24	23	20	18	18
ABCG2	5NJG	3654	-	3.78	Nanodisc (MSP1D1)	20	19	17	16	15	15
	6ETI	3953	-	3.1	Nanodisc (MSP1D1)	19	19	17	16	14	14
	6FEQ	4246	-	3.6	Nanodisc (MSP1D1)	31	31	27	25	22	22
	6FFC	4256	C2	3.56	Nanodisc (MSP1D1)	29	28	26	25	25	24
	6HCO	196	C2	3.58	Nanodisc (MSP1D1)	33	32	31	28	28	26
	6HZM	190	C2	3.09	Nanodisc (MSP1D1)	26	25	23	23	22	22
ABCA1	5XJY	6724	C1	4.10	Digitonin	35	31	28	27	26	25
LptB2FGC	6MI7	9125	C1	4.2	Nanodisc (MSP1D1)	28	25	23	22	21	20
	6S8N	10125	C1	3.10	LMNG	22	19	18	18	16	14

GPCR	5UZ7	8623	C1	4.1	MNG/CHS	36	30	28	27	22	21
	6B3J	7039	C1	3.3	MNG/CHS	30	27	24	24	17	17
	6CMO	7517	C1	4.5	Digitonin	35	32	32	30	30	28
	6D9H	7835	C1	3.6	LMNG/CHS	23	22	19	19	17	16
	6E3Y	8978	C1	3.3	LMNG/CHS	24	20	18	16	13	13
	6G79	4358	C1	3.78	DM	22	21	20	19	16	15
	6N4B	0339	C1	3	LMNG/GDN	29	27	26	26	25	24
	6NBF	0410	C1	3	LMNG/GDN/CHS	36	36	32	29	28	27
	6NI3	9376	C1	3,8	LMNG	21	19	19	18	17	16
	6OIJ	20078	C1	3,3	LMNG/GDN	26	26	23	20	20	19
	6OIK	20079	C1	3,6	LMNG/GDN	33	31	31	28	27	22
	6OS9	20180	C1	3	LMNG/GDN	25	25	24	23	20	18
	6OT0	20190	C1	3,84	MNG/GDN/ CHS/ Digitonin	31	31	30	29	28	22
	6OY9	20222	C1	3,9	LMNG	24	24	24	21	20	16
	6PWC	20505	C1	4,9	Digitonin	38	36	34	30	29	29
	6QNO	4598	C1	4,38	-	21	17	16	15	15	13

1
2